Construction and test of a modular Time Projection Chamber with MPGD amplification for the measurement of field distortions

D. Schaab*, R. Beck, P. Hauer, B. Ketzer

Forschungs- und Technologiezentrum Detektorphysik, Universität Bonn, Kreuzbergweg 24, D-53115 Bonn, Germany

Abstract

In the context of gaseous detectors, present studies on amplification components as well as the investigation of energy resolution and charging-up effects are often performed with test detectors which do not provide spatial information. This is connected to the fact that it requires more channels and a more sophisticated build-up with limited access to exchange single components. Motivated by the latter, a tracking detector called *small Time Projection Chamber* (sTPC) has been developed with focus on mechanical handling and modularity: the comparably simple exchange and test of its components provides a straightforward access to more differentiated measurements and a better understanding of observed phenomena in Micro Pattern Gaseous Detectors (MPGD). The sTPC enables the test of various detector components, as amplification structures or frontend electronics, on a small scale. The tracking chamber is designed for standard-sized $10 \times 10 \, \text{cm}^2$ amplification structures established by the CERN Gaseous Detector Development group (GDD). In the present configuration it uses a hexagonally segmented padplane combined with readout electronics using the AFTER-chip and a DAQ equivalent to the one used by the FOPI-TPC at GSI [1]. With regard to high-rate capabilities of time projection chambers at collider experiments, it was of interest to investigate a photoelectric field calibration concept which was taken into account in the current design of the sTPC. Motivated by this, it was one main goal to measure field distortions in [2]. In this context, laser light was conditioned and guided through various

optical components and a bundle of opical multimode fibers in order to illuminate the detector cathode sufficiently uniform. The detector build-up as well as an optical setup, containing a deep-ultraviolet-laser (DUV-laser) and fiber bundle, will be thematized. In order to generate artificial field distortions the field configuration inside the detector was misadjusted

---

1. Introduction

- Gaseous detectors R&D

    - limited access to test detectors with position resolution

        * no established test-scale tracking detector with exchangeable MPGD structures

        * MPGD structures as GEMs or MMs are often studied locally (gain, ion backflow, charging-up, ...)

    - gaseous detector designs do often contain irreversibly connected parts (glued junctions)

        * debugging more difficult

        * part exchange for comparable measurements more difficult

- Field distortion studies especially involving photoelectric effect or other preparations of the cathode

    - require reversibly dismountable cathodes

    - require readout with spatial resolution

    ⇒ Development of fully modular tracking chamber sTPC

        - for standard-sized $10 \times 10\,\mathrm{cm}^2$-GEMs or other MPGDs established by GDD

2

- minimum amount of glued junctions

   - hexagonally segmented readout structure

  - manipulable cathode and field cage

2. General Design

- All relevant parts shown in figure 1 / listed in table 2

- FOPI-TPC [1] readout structure, electroncis and operational gas(es) used
  als inspiration

- Detector build-up

  - cylindric aliminum body with flanges for window end-cap, side window and readout end-cap

    * internal cylindric support for field cage of coppered polyimide (photolithographic production), field strips connected via resistor chain (see 2) to achieve homogeneous field in the sensitive region of the detector

    * three mounting threads at side of body

  - window cap (o-ring-sealed) with double-sided coppered polyimide window and cathode (photolithographic production)

    * cathode separated from window to avoid warping due slight detector over pressure and to avoid instability of cathode position due to pressure variations

    * gap between window and cathode chosen such that no gas amplification in Ne/CO_2 (90/10) can take place when cathode at nominal voltage of $8\,kV$

    * window and cathode foils enable entrance of radiation for measurement and calibration purposes

  - side window cap (o-ring-sealed) for aliminized Mylar-window
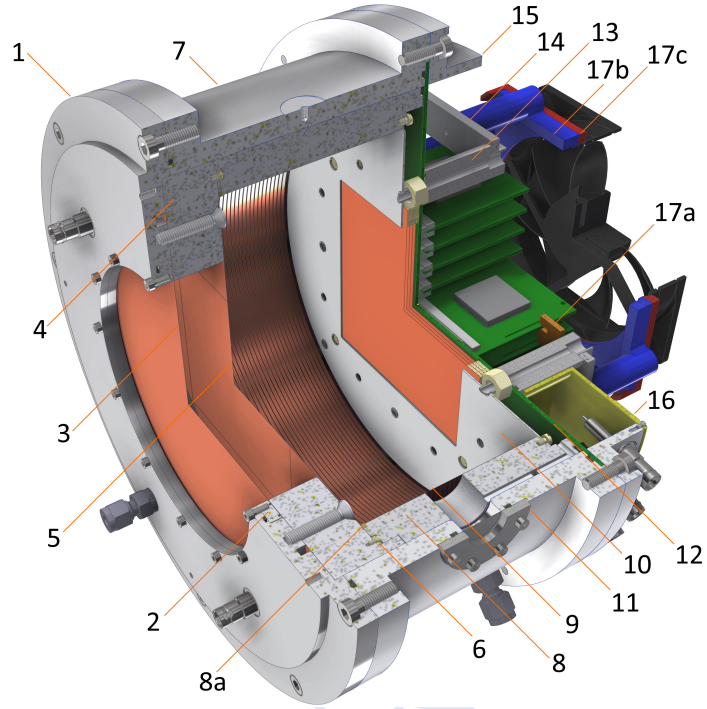
Figure 1: CAD sketch of the sTPC [2] with numbered parts itemized in table 2

45   – readout end-cap (o-ring-sealed)

           * gas-tight PCB with hexagonally segmented readout pads and GEM high voltage supply (see section 5)

           * press-on-ring with SHV connector jacks

           * eight frontend cards with air cooling

50   • Electronics and data acquisition (see section 7)

        – T2K-AFTER readout electronics [3]

        – modified GEM-APV data acquisition chain from COMPASS experiment (see [4, 1])

4

Table 1: Design parameters of the sTPC with default GEM-optimized readout plane.

parameter	value	unit
outer dimensions		
outer diameter	300	mm
total length (with periphery)	174 (291)	mm
active volume		
xy dimensions (square area)	100×100	mm
z dimension (drift length)	99.7	mm
active volume	1.0	L
further dimensions		
total gas volume (active + inactive)	~ 4.3	L
distance readout - skirt (center plane)	$10.0^{+0.1}_{-0.0}$	mm
distance readout - last strip (center plane)	$13.5^{+0.1}_{-0.0}$	mm
distance skirt - last strip (center plane)	3.5	mm
GEM amplification stage		
effective gain (operated)	$1k \sim 100k$	
GEM thickness	60	µm
GEM pitch	140	µm
GEM hole	70	µm
GEM stack height max.	9.5	mm
no. GEMs max. (used)	4 (3)	
transfer gaps	variable	
induction gap	variable	
electronics		
no. of readout pads	2016	
no. of veto pads (not used here)	32	
ASIC	T2K-AFTER	
sampling clock	19.44	MHz
buffer depth	511	
no. of frontend cards	8	
ADC resolution	11	bit
sensitivity [1]	393	e^-/ADC

Table 2: Part list of the sTPC with specification of material and manufacturing process. The part numbers correspond to figure 1.

part group	no.	designation	material	fabrication
enclosure (cath.)	1	lid plate	Al	PM
	2	press-on ring, window	Al	PM
	3	window foil	PI, Cu	PL, ext
	4	distance ring	PTFE	PM
	4a	HV contact (press-fit)	Al	PM
	5	cathode foil	PI, Cu	PL, ext
	6	cathode support ring	GRP	PM
corpus	7	corpus	Al	PM
	8	field cage support	PC (here: POM)	PM
	8a	cathode contact ring	CuZn (brass)	PM
	9	field cage foil	PI, Cu	PL, ext
	10	skirt	VA, sheet	PM
	11	press-on ring, side window	VA	PM
readout	12	readout board	FR4, Cu etc.	PL, ext
	13	fiber bundle ferrule	POM	PM, ext
		fiber bundle dummy (altern.)	POM	PM
	14	orientation frame	Al	PM
	15	press-on ring, readout	Al	PM
	16	HV protection	3D print	3D
	17a	comb guide for readout	3D print	3D
	17b	fan spacer	3D print	3D
	17c	fan mounting structure	3D print	3D
stretch. frame window	A	stretching frame	PMMA	PM
	B	stretching frame	PMMA	PM
	C	weight	VA	PM
stretch. frame cath.	D	stretching frame	PMMA	PM
	E	stretching frame	PMMA	PM
	F	weight	VA	PM

3. Field Cage

- Motivation

    - Keep electric field homogeneous in the sensitive volume

    - set defined field at the boundaries of the detector

- Principle

    - the field between cathode and readout area would behave similarly to a finite parallel plate capacitor with outbreaking field lines at the boundaries. Moreover, the grounded metallic enclosure would distort the field inside the capacitor even more.

    - field cage: equidistant metallic strips between readout structure and cathode connected via a chain of equal resistors

    - a constant current by the chain creates a defined stepwise voltage drop at the boundaries of the detector

    - the spatial size of field inhomogeneities reduces roughly to the size of the strip distance, but only at the field cage itself. The bulk of the detektor volume stays homogene

- realization

    - coppered ($5\,\mu$m) polyimide foil ($50\,\mu$m) produced in a photolithographic process (see figure 2)

    - solder pads assembled with $10\,$MΩ-resistors

    - foil gets glued on field cage support[1]

    - field cage support contains a notch to embed resistor chain. Resistor chain gets covered with other end of field cage foil by wrapping it around

---

[1]support made of POM; before gluing pre-treatment with fine sand paper necessary (e.g. for Araldite 2011)
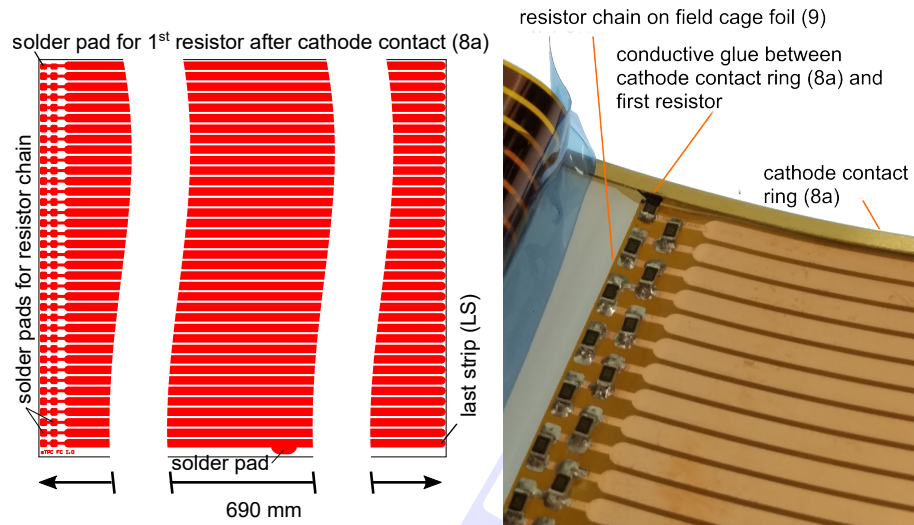
7

Figure 2: Cropped image of the Gerber representation of the field cage and photograph of the same sitting on the support and having resistor chain assembled. The uppermost resistor gets glued to the pressed-in cathode contact ring. From [2].

      – strip next to cathode: gets connected via $10\,\mathrm{M\Omega}$-resistor to contact ring sitting on support structure, conductive glue is used

- dimensions

      – length $690\,\mathrm{mm}$

      – number of strips: 37, strip width: $2\,\mathrm{mm}$, clearance: $0.2\,\mathrm{mm}$

4. Cathode and Skirt

- cathode

      – produced in a photo-lithographic process, double-sided coppered, inner side segmented

            * copper surface facing away from the sensitive volume avoids charging-up effects by charges potentially created by radiation between window and cathode

8

* copper surface facing towards sensitive volume is segmented in square inner area above the detection sensitive region and an outer area to be able to distinguish currents in ion backflow measurements

— conductive junction to the field cage is realized by glue- and solder-
less connection via a contact ring on the field cage support structure (see figure 2). This simplifies the disassembly of the window end-cap.

- skirt (part 10 in figure 1)

— opposite to the cathode, one finds the amplification stage realized by a square-shaped GEM-system serving as amplification stage right
before the segmented readout plane. The skirt is a sheet metal that surrounds the the square-shaped readout region kept at a defined potential

— shields the inner drift field from perturbing potentials from the pad-plane PCB

— keeps the drift field largely homogeneous. In 9 the influence of the skirt potential on the homogeneity is discussed.

5. Padplane

- Geometry (see figure 4)

— hexagonal geometry adjoined to FOPI-TPC [1], chosen due to good
geometry in terms of isotropy of track reconstruction (e.g. compared to square geometry) and straightforward understanding of neighboring pads (same distance to all neighbors)

— pad geometry dimensions generated by constraints

* following the results of a simulation including diffusion in [1], the
optimal pad size is at $1.0\,\mathrm{mm} \lesssim r_{\mathrm{pad}} \lesssim 1.5\,\mathrm{mm}$ (see figure 3)

* square-shaped boundary: standard-sized $10 \times 10\,\mathrm{cm}^2$ GEM as amplification stage

* number of available channels on eight T2K-AFTER frontend cards, containing 256 channels per card (4 channels per card / 32 total used for veto signals)

– active readout contains 2016 pads with outer radius $r_{\mathrm{pad}} \equiv a = 1.39\,\mathrm{mm}$

– active readout structure surrounded by ring of larger pads which can be used as veto-pads in order to detect incomplete clusters

• Realization (see figure 5)

– regard gas-tightness

* PCB with plugged and tented vias

* 4-layer routing without direct vias (routing through inner layers) to improve gas tightness

– Pads routed from top side to eight connectors of type `BTH-150-X-D-X` on bottom side to match T2K-AFTER frontend v7.15

– high voltage supply for amplification stage

* high voltage supply for e.g. up to four $10 \times 10\,\mathrm{cm}^2$-GEMs established by CERN GDD

* if accordingly prepared, high voltage flaps can be soldered directly to the PCB avoiding additional small un-isolated wire structures which could cause corona discharges

* loading resistors are foreseen on the PCB

* attention was paid to comply with distances of tracks at different high voltage potentials in terms of dielectric strength (integrated in design rules of routing software)

* two spring-loaded contacts foreseen for skirt contact and the contact of the field cage last strip in order to simplify the disassembly
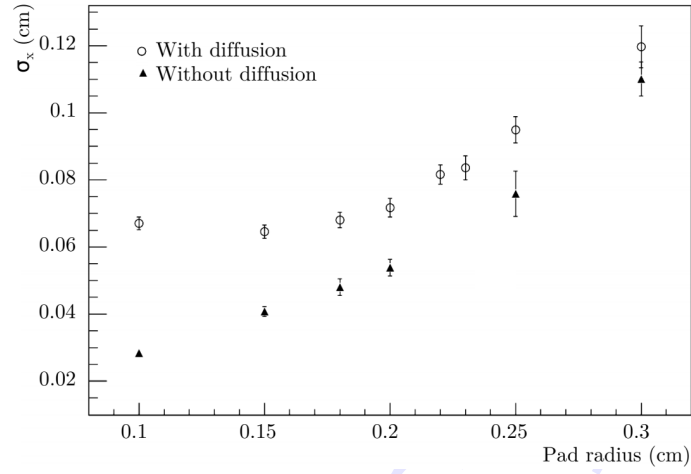
10

Figure 3: Position reconstruction accuracy vs. pad radius derived from Monte Carlo simulations with Ne/CO_2 (90:10) at a magnetic field of $2\,T$. From [1].

of the readout end-cap, i.e. no soldering is required to remove the readout PCB

– optical fiber feed-through

   ∗ eight drills (8 mm diameter) surrounding readout area for optical fibers foreseen; can be replaced by dummies if not required
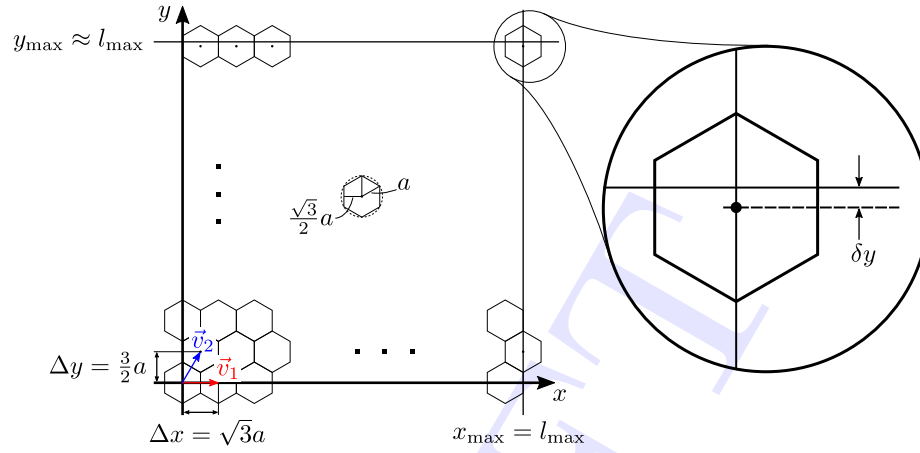
   ∗ to achieve gas-tightness, o-rings must be used

11

Figure 4: Geometrical construction constraints for the hexagonally segmented padplane with $l_{\max} = 100\,\mathrm{mm}$. From these, a pad radius of $r_{\mathrm{pad}} \equiv a = 1.39\,\mathrm{mm}$ is derived. Displacement parameter $\delta y = 1.92\,\mathrm{mm}$. From [2].
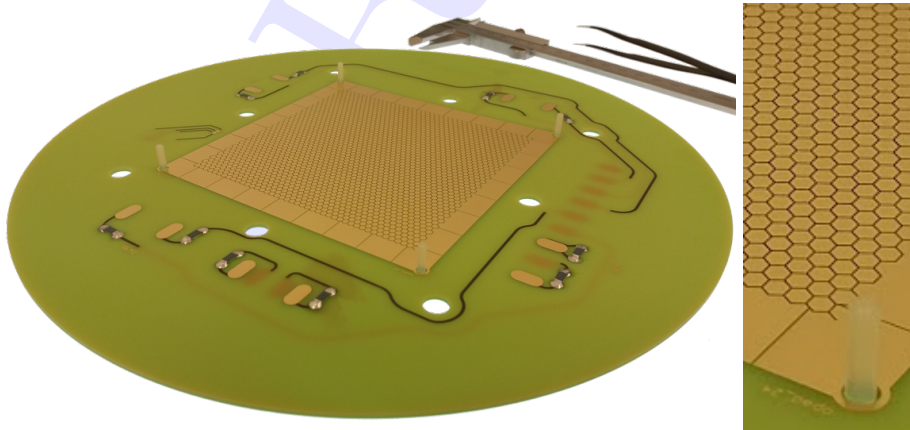
Figure 5: Photograph of the padplane [2].

6. Gas Flow

- the gas path was chosen such that all parts of the detector get flushed and gas pockets are avoided in order to improve the gas quality in a constantly flushed open-system detector

- gas path (see figure 6)

  - gas entering through 6 mm Swagelok ferrule next to the amplification stage

  - flowing through holes in skirt and gaps between skirt and amplification stage into the drift region

  - exiting through hole in cathode and spacer ring in the cavity between cathode and window foil

  - exiting window end-cap cavity and flushing all other cavities in the lid plate in order to avoid gas pockets

  - exiting lid plate through 6 mm Swagelok ferrule

13
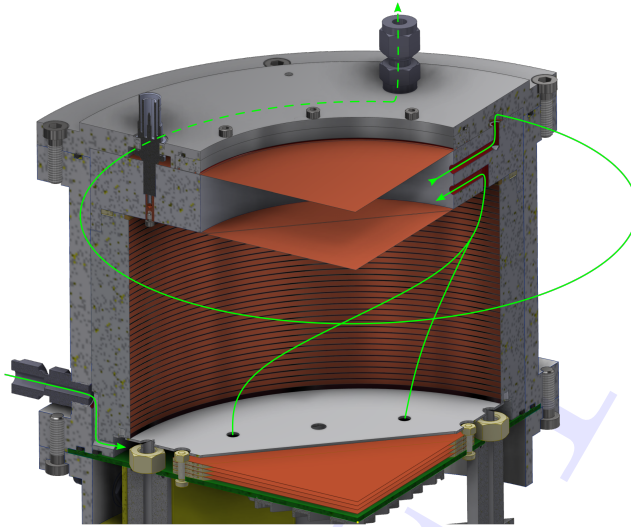
Figure 6: Schematic gas flow in the sTPC [2]. The gas is guided through most of the cavities in the detector to avoid enclosures.

7. Electronics and Data Acquisition

- The used electronics and data acquisition system is a down-scaled version of the FOPI-TPC which can be looked up in [1], a block diagram can be found in figure 7

- frontend electronics

  - 8 T2K-AFTER [3] frontend cards with 4 ASICs each having 64 channels (256 total per card)

  - integrated circuit containing

    * charge sensitive amplifier (CSA) converts integrated charge to a voltage step

    * shaping amplifier limits the pulse width and filters noise components

    * switched capacitor array (SCA) stores the time-sampled signal using an analog buffer array of the size 511

14
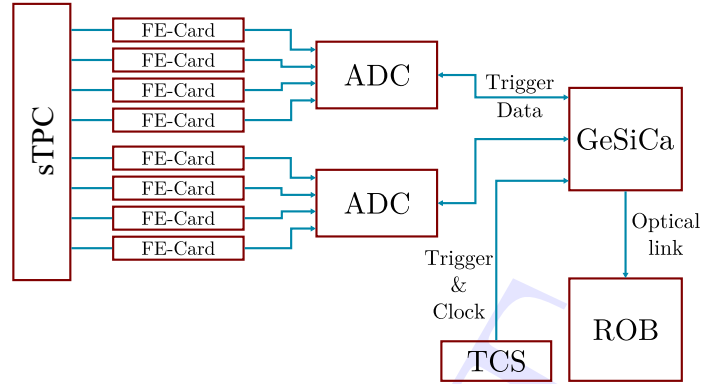
Figure 7: sTPC readout scheme. The signals from the GEM-TPC are sampled by the front-end (FE) cards and digitized by the analog-digital converters (ADC). The ADCs send their data to the GEM-Silicon Control and Acquisition (GeSiCa) boards. Finally, all data are collected in the read-out-buffer (ROB) computer. The trigger and clock is controlled by the Trigger Control System (TCS) and distributed via the GeSiCas to the ADCs and from there to the frontend cards. Figure and caption from [1], modified.

* the capacitor array signal is multiplexed and sent out serially on a differential line via flat cable towards a digitizing unit

digitization

– 2 sampling ADC boards (1 per 4 frontend cards) running at a read sampling speed of 20 MHz convert the beforehand serially sent out data to digital values (11 bit)

– at this stage, the single samples in time correspond to individual input channels of the ASIC and with it to individual pads

8. Photoelectric Field Calibration Setup

- In high-rate experiments, high amounts of space charges can be created in the sensitive drift region leading to field inhomogeneities. The origin of these charges is mainly the amplification stage right before the readout where a fraction of ions is drifting back from. The resulting effective

15

space charge itself leads to distortions of the measured tracks which finally results in a degradation of the spatial resolution of the tracking chamber.

- An ansatz to correct for this systematic effect is to find a measure of the spatial displacements created by field distortions and correct for it. A concept with comparably low expense is the photoelectric field calibration where the cathode is prepared with photo-sensitve structures (e.g. dots and strips) and illuminated with (UV)-light in order to release photoelectrons at defined positions. Being deflected from their original in-plane-position, these electrons drift towards the readout structure and show the integral field inhomogeneities. The concept is illustrated in figure 8.

- In combination with simulations at different collision rates and a deterministic effective space charge the measurement of the displacement can help to correct for the field distortions.

- Another issue is that drift velocity as well as the detector gain depend on variations of T/p and gas composition which one can correct for by a drift velocity measurement on the one hand and a gain monitoring measurement on the other hand

- Realization of field calibration concept

    – preparation of the cathode with photosensitive material. Here, aluminum an pattern on a copper bulk material has been used. The aluminum pattern has been deposited in a vacuum evaporation technique, using a negative-mask made of $330\,\mu m$ brass sheet metal (see figure 9).

    – illumination of the cathode with light and making use of the photoelectric effect.

        * deep-UV laser light of $266\,nm$ has been used overcome the work function threshold of aluminum

* laser light from a pulsed laser has been expanded and conditioned such that it can be coupled through a diffuser into an optical multimode fiber-bundle of 684 single fibers manufactured by Ceramoptec. The bundle is divided into eight sub-bundles which are gas-tightly mounted to the detector's readout PCB.

* by the bundle, the light is transported into the detector where it is supposed to illuminate the cathode sufficiently homogeneously. A simulation has been developed to predict the illumination profile at the cathode depending on the grinding angles at the ends of the fiber bundles. Measured maps of optical energy per area $\mathrm{d}E/\mathrm{d}A$ at the location of the cathode plane is shown for two different diffusers (before the light coupling into the fiber bundle) in figure 11

– The setup including the optical components is illustrated in figure 10.

– creating field distortions

* one simple way to introduce field inhomogeneities using present detector components is to disadjust the potential of the skirt (see figure 1, part 10). Different voltage polarities relative to the nominal skirt potential lead to different directions of displacement of the probe electrons (see figure 14)

* another possibility is to illuminate the drift volume with a high-intensity x-ray source, which was not done in the scope of the project

• Realization of the drift velocity calibration

– Knowing the triggering time of the laser and the propagation times of the DAQ system, it is possible to measure the drift time of photo-electrons which were released by a laser pulse which is significantly shorter than the required precision of the drift time.
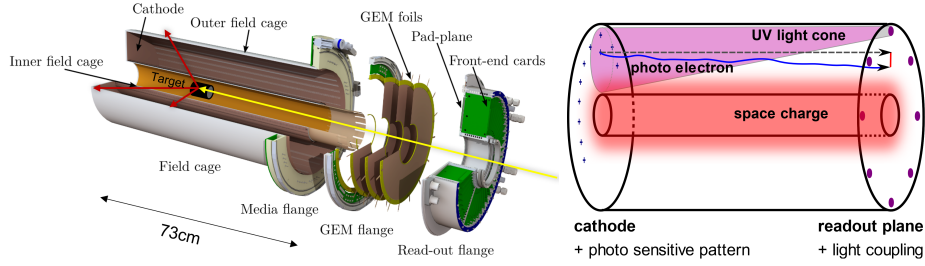
17

Figure 8: Left: drawing of the FOPI-TPC with an illustrated target in the center – from [1], modified. Right: illustration of the photoelectric calibration concept at given detector geometry with an effective space charge e.g. at high-rate measurements – from [2], modified.

– For the analysis of the data it is benefitial to know the response function of the readout electronics in order to reconstruct the signal response time correctly

- Realization of the gain monitoring (not treated here)

  – This topic has not been treated yet, neither in this paper nor in [2]. But in principle it can be easily proven, once the detector setup has been realized by having a reference x-ray calibration running in parallel, e.g. with the help of a ^{55}Fe-source

  – A degradation of the photosensitive material during the measurement time has to be excluded such that on average the same amount of photo-electrons can be expected from certain calibration structures on the cathode

  – Moreover, the laser intensity has to be monitored at the same time since lasers often have a strong environmental dependence, especially on the temperature
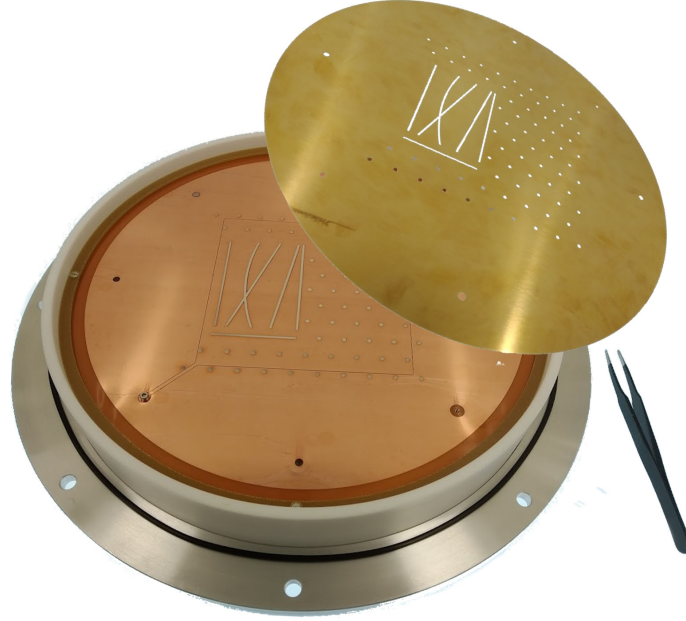
18

Figure 9: Copper cathode of the sTPC with aluminum calibration pattern deposited in a vacuum evaporation technique. As mask negative, a stencil of $300\,\mu m$ brass sheet metal has been used.
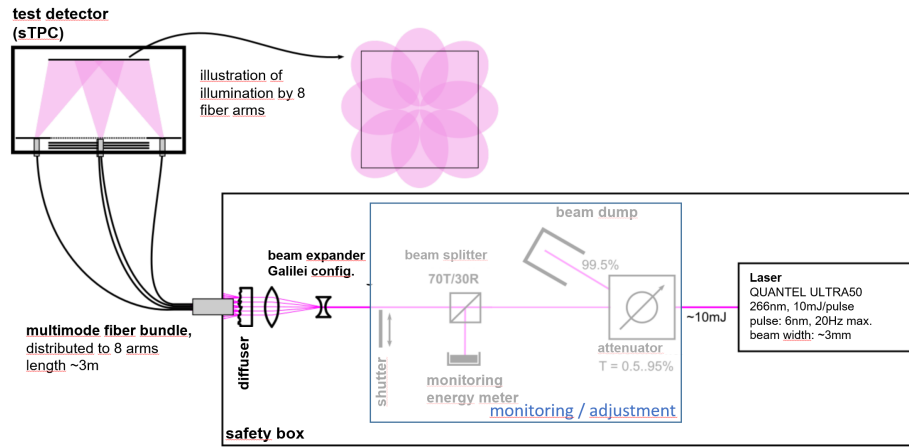

Figure 10: Block diagram of the photoelectric field calibration setup using a deep-UV-laser, components for the beam conditioning. From [2], modified.
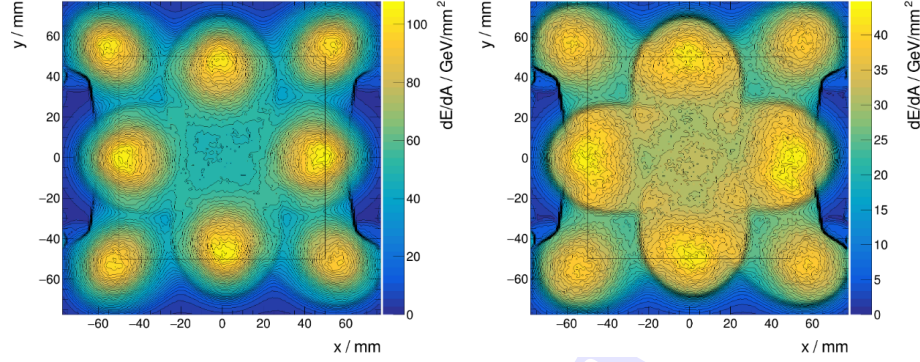
Figure 11: Determined optical energy per area per laser shot at the cathode plane from measured data [2]. Knowing the work function (distribution) of the structures on the cathode plane, the amount of photo-electrons can be calculated in a certain area. Two different diffusers at the input of the multimode fiber bundle have been considered. Left: sandblasted diffuser, right: holographic diffuser. The sensitive detector area of $10 \times 10 \, \mathrm{cm}^2$ is illustrated as square line.

9. Commissioning and Applications

- As motivated and described in the previous section 8 a detector setup has been realized to achieve two main applications

  – creation of field distortions and finding a way to quantify them

  – a drift velocity calibration

- In figure 12, the fully equipped sTPC is shown, including the eight fiber bundle arms mounted to the readout PCB. The following subsections show the main results of these applications.

9.1. Field distortions

- The laser setup illustrated in figure 10 has been used to illuminate the cathode plane sufficiently homogeneous. Since a sandblasted diffuser was used to couple into the fiber bundle (see section 8), the intensity profile corresponds to the left plot in figure 11.
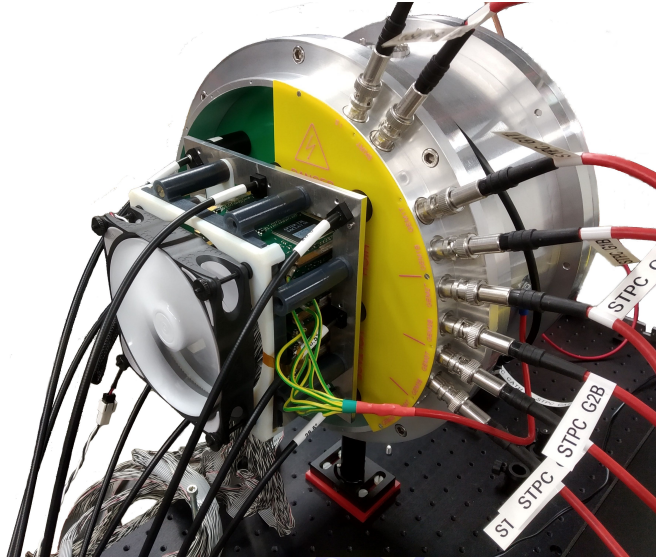
20

Figure 12: Photograph of the fully equipped sTPC. From [2].

- The layout of the photosensitive pattern on the cathode – described in section 8 – is shown in figure 13 (left).

- By the illumination of the cathode using a single laser shot of $\sim 6\,\text{ns}$ a spatially resolved signal is created at the readout plane. This signal is superimposed at the right picture of figure 13 which already confirms the photoelectric response.

- By the misadjusting the skirt potential (see figure 1, part 10) with respect to its nominal value, one can introduce massive field distortions, especially at the edges of the sensitive regions. Two cases of oppositely tuned skirt potentials are shown in figure 14. Systematic displacements and standard deviations of statistical reconstruction uncertainties are depicted as red arrows and ellipses, respectively. For the plots, those quantities are magnified by a factor of 10.

- The results are a proof of principle for the photoelectric field calibration in the given configuration.
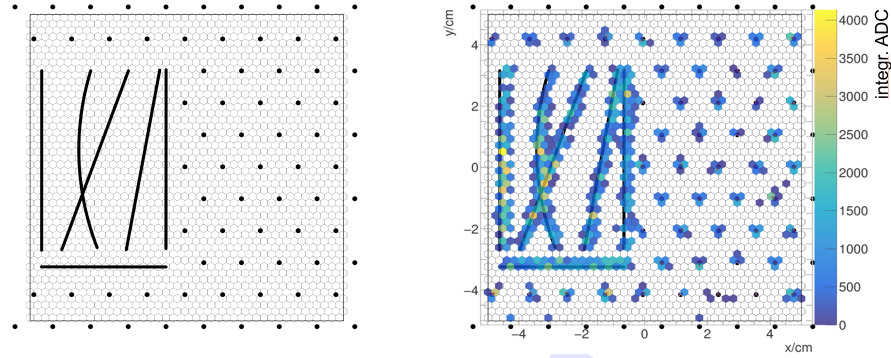
21

Figure 13: Layout of the photoelectric calibration pattern and superimposed measured signal taken from a single laser shot as proof priciples. Signal measured in uncalibrated ADC values. Data taken in the scope of [2]. The square line shows the sensitive area of the detector which is $10 \times 10\,\mathrm{cm}^2$.

- With the given setup (calibration dot radius $r_{\mathrm{dot}} = 2\,\mathrm{mm}$, outer readout pad radius $r_{\mathrm{pad}} = 1.39\,\mathrm{mm}$, gas mixture $\mathrm{Ar/CO_2}$ (90/10), field configuration 97 % of the standard field settings in [2]), it is possible to quantify the statistical reconstruction uncertainty to be [2]

$$\sigma_x = (359 \pm 8)\,\mathrm{\mu m}$$
$$\sigma_y = (372 \pm 8)\,\mathrm{\mu m}.$$

It has to be kept in mind that pad geometry and calibration dot size as well as the transversal diffusion in the gas play a role. But the result shows that a reconstruction precision is possible which is clearly below the readout pad size.

- For vividness, figure 15 shows in color scale the accumulated photoelectric signals of 2500 single illuminations of one calibration dot against the position in x and y. Moreover, the reconstruction positions of the single illuminations are shown as black dots. The size of the dot cloud is a measure for the reconstruction position given by a single illumination.
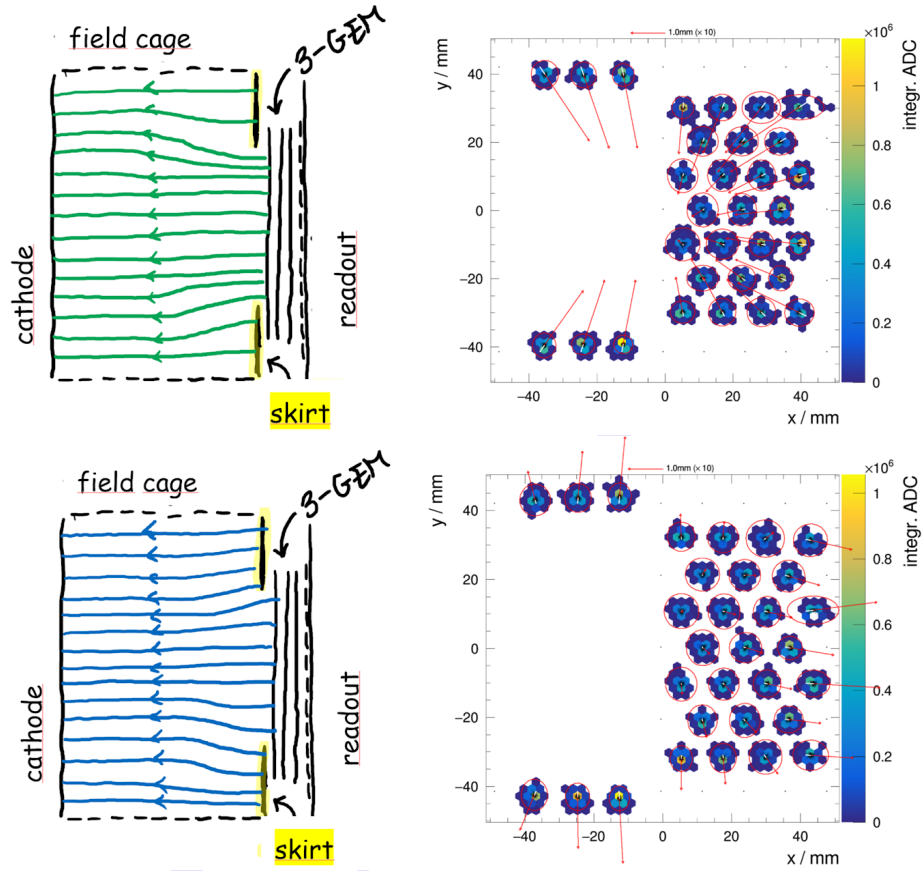
9.2. Drift velocity calibration

Figure 14: Two different cases of a disadjusted cathode potential. It can be either achieved a focusing or a de-focusing effect. The displacements with respect to the expected dot positions and the standard deviations are visualized as red arrows and ellipses, respectively. Both are magnified by a factor of 10. Per readout pad the, ADC values are integrated over all samples. Data from [2].
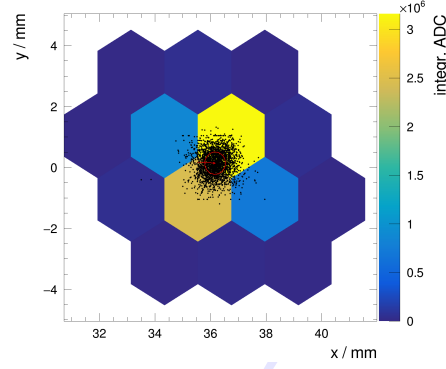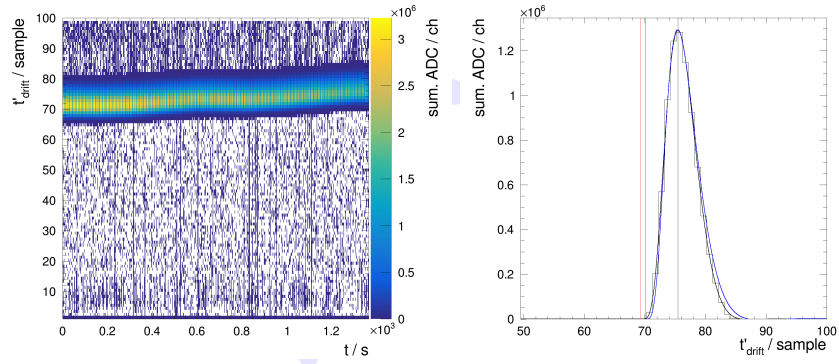
Figure 15: Enter Caption

Figure 16: Preparation of the drift velocity calibration: within the shown time window of the left plot, the pressure inside the detector has been varied in a range of $\sim 53\,\mathrm{mbar}$ which has direct impact on the drift time – here, represented in samples. The temperature has been kept nearly constant during the measurement. The right plot shows an example slice in the tenth time bin. From [2].
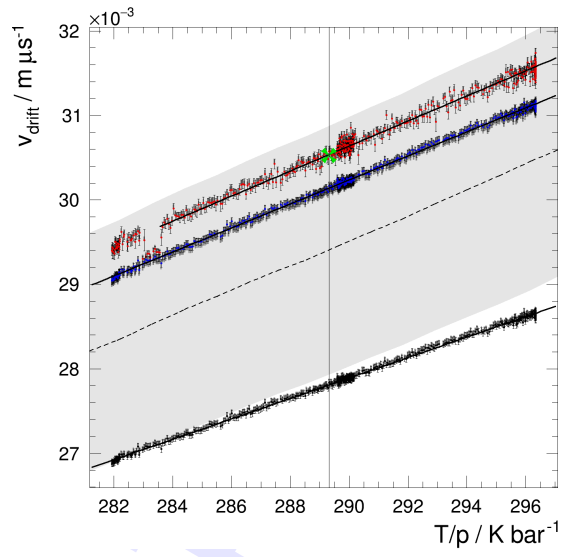
Figure 17: Drift velocity calibration for different values of T/p compared to data (dashed line with gray error band) derived from [5]. The blue and red data points correspond to the equally colored vertical lines in figure 16 which represent different signal arriving times dependent on the choice of the response function. Here, the red data represents the best approximation. As reference, the approximated peak time is plotted as well in black.

References

[1] M. Berger, M. Ball, L. Fabbietti, B. Ketzer, R. Arora, R. Beck, F. Böhmer, J.-C. Chen, F. Cusanno, S. Dørheim, F. García, J. Hehner, N. Herrmann, C. Höppner, D. Kaiser, M. Kis, V. Kleipa, I. Konorov, J. Kunkel, N. Kurz, Y. Leifels, P. Müllner, R. Münzer, S. Neubert, J. Rauch, C. Schmidt, R. Schmitz, D. Soyk, M. Vandenbroucke, B. Voss, D. Walther, J. Zmeskal, A large ungated tpc with gem amplification, Nuclear Instruments and Methods in Physics Research Section A: Accelerators, Spectrometers, Detectors and Associated Equipment 869 (2017) 180–204. doi:https://doi.org/10.1016/j.nima.2017.05.027.
URL https://www.sciencedirect.com/science/article/pii/S0168900217305739

[2] D. Schaab, Entwicklung einer Spurkammer für das Studium von Driftfeld-Kalibrationsmethoden, Ph.D. thesis, Rheinische Friedrich-Wilhelms-Universität Bonn (Jun. 2022).
URL https://hdl.handle.net/20.500.11811/9866

[3] P. Baron, F. Druillole, M. Zito, A. Le Coguie, X. de la Broise, E. Monmarthe, A. Delbart, J. Beucher, D. Calvet, E. Mazzucato, et al., After, the front end asic of the t2k time projection chambers (2009).

[4] B. GRUBE, R. De Masi, J. Friedrich, I. Konorov, S. Paul, L. Schmitt, F. Simon, R. WAGNER, M. Wiesmann, B. Ketzer, Architecture of the common gem and silicon readout for the compass experiment (11 2002). doi:10.1142/9789812776464_0040.

[5] W. N. English, G. C. Hanna, Grid ionization chamber measurements of electron drift velocities in gas mixtures, Canadian Journal of Physics 31 (5) (1953) 768–797. arXiv:https://doi.org/10.1139/p53-070, doi:10.1139/p53-070.
URL https://doi.org/10.1139/p53-070